



# Instrument for fast whole-field peripheral refraction in the human eye

ENRIQUE J. FERNANDEZ,<sup>1,2</sup>  SANTIAGO SAGER,<sup>1,2</sup> ZHENGHUA LIN,<sup>1,3</sup>  JIANGDONG HAO,<sup>3,4</sup> JAVIER ROCA,<sup>2</sup> PEDRO M. PRIETO,<sup>1,2</sup>  ZHIKUANG YANG,<sup>3,4,5</sup> WEIZHONG LAN,<sup>3,4,6</sup>  AND PABLO ARTAL<sup>1,2,3,7</sup> 

<sup>1</sup>Laboratorio de Óptica, Centro de Investigación en Óptica y Nanofísica (CiOyN), Universidad de Murcia, Campus de Espinardo (Ed. 34), 30010 Murcia, Spain

<sup>2</sup>Voptica S.L., Parque Científico de Murcia, Ctra. de Madrid 388, Complejo de Espinardo – Edificio T, 30100 Murcia, Spain

<sup>3</sup>Aier School of Ophthalmology, Central South University, 410000 Changsha, China

<sup>4</sup>Aier School of Optometry and Vision Science, Hubei University of Science and Technology, 437100 Xianning, China

<sup>5</sup>Yangzhikuan@aierchina.com

<sup>6</sup>lanweizhong@aierchina.com

<sup>7</sup>pablo@um.es

**Abstract:** An instrument for fast and objective measurement of the peripheral refraction in the human eye is presented. The apparatus permits the automatic estimation of both defocus and astigmatism at any retinal eccentricity by scanning a near infrared beam. The design includes a Hartmann-Shack wavefront sensor and a steering mirror, which operate in combination with a compounded eyepiece for wide field operation. The basic scanning protocol allows the estimation of refraction in a circular retinal patch of 50 deg diameter ( $\pm 25$  from central fixation) in 3 sec. Combined with additional fixation points, wider retinal fields can be sampled to achieve a whole field. The instrument underwent calibration and testing, and its performance for real eyes was assessed in 11 subjects of varying age and refraction. The results show high repeatability and precision. The instrument provides a new tool for the investigation of peripheral optics in the human eye.

© 2022 Optica Publishing Group under the terms of the [Optica Open Access Publishing Agreement](#)

## 1. Introduction

Peripheral optics and vision play an important role in different situations. For example, it is known that peripheral vision is of importance in mobility: some tasks as driving [1–3], walking [4–6], and practicing certain sports [7–8] are greatly affected by the capability of the visual system in the periphery. Additionally, peripheral vision provides the only visual information for those patients suffering from retinal conditions compromising the foveal area, such as, e.g., macular degeneration [9,10]. Consequently, measurement and correction of peripheral refractive errors may be of importance for these patients [11,12]. Aside of these vision-related applications, much of today's interest in the study of peripheral refraction arises in the context of myopia control. Myopia is known to be associated to a different shape of the posterior eye as compared with the emmetropic eye, affecting the morphology of the retina [13,14]. Whether the changes in relative retinal shape, the profile compared with central fovea, are cause or consequence of myopia progression remains controversial. The subject offers a promising research line to better understand the myopia onset [15,16, 17], and eventually a means to halt its progression through interventions affecting peripheral refraction.

Peripheral refraction has been measured for more than 90 years [18]. Subjective refraction in the periphery involves the display of visual charts off axis, occasionally in combination with

trial lenses. Since the peripheral retina exhibits a significant reduction in visual performance as compared to foveal vision, these are more complicated tasks as in normal refraction. In addition, subjective methods rely on the ability of the patient to maintain fixation, involve continuous change of position of the visual test for sampling different eccentricities, and bring about significant protraction, all of which may affect the performance of the subjects [19]. While subjective refraction is still considered as the gold standard for central, foveal vision, in the periphery, objective methods, requiring little or no cooperation from the patient, are advantageous [20].

Along the years, several objective techniques have been used for peripheral refraction estimation, for instance retinoscopy [18,21–23], double-pass retinal imaging [24–29], autorefractors, including commercial models [30–33], and photorefractometry [34]. All these modalities require the subject to change the line of gaze to obtain the refraction at different eccentricities. This circumstance makes them unfeasible for high sampling of the retinal field, and to certain extent, unreliable. Their accuracy is based on the subject's ability to maintain fixation for extended periods of time.

A major advance in the determination of peripheral refraction has been the use of wavefront sensors. Among them, the Hartmann-Shack (H-S) sensor is the most widely used technology [35]. Several studies have used laboratory H-S instruments for estimating peripheral refraction, in some cases comparing the method with other techniques [36–40]. The results show in general that the H-S based approach surpasses the alternatives in precision and reliability. Despite the evident advantage of this class of instruments, including commercial aberrometers, they share in most cases the main limitation of other techniques: they require changing the fixation point to retrieve refraction at different eccentricities, which limits the number of points across the retinal field that can be sampled. An alternative to this cumbersome approach is to keep the subject's fixation steady and perform an angular scan with the measurement beam. A first antecedent in this direction achieved  $\pm 15$  deg scanning of the retinal field in approximately 7 s [41]. Two other instruments, combining the H-S sensor with opto-mechanical relays, have been developed to circumvent some of the limitations of this approach. In the instrument of Jaeken et al. [42,43], the relay containing the sensor mechanically rotated around the eye of the subject, who maintained the gaze to a fixation point projected in open view in front of the apparatus. The refraction along the horizontal meridian could thus be estimated. By changing the height of the fixation point, horizontal scans at other eccentricities in the vertical direction could be sampled to complete a 2D mapping of refraction [44]. Despite its potential, the instrument presented some drawbacks, namely the difficulty in centering the subject and the need of multiple scans for every different fixation point. In other apparatus combining H-S technology with scanning capabilities [45], a set of prisms directed the wavefront emerging from different retinal locations along a meridian to an H-S wavefront sensor. The instrument exhibited certain limitations in its range, selection of meridians, and the density of sampling points.

Despite the vast number of techniques and instruments developed along the years, there are still important challenges to determine in practice the peripheral refraction. In this work, we present a new instrument, combining an H-S wavefront sensor with a scanning laser beam, to obtain the refraction at any retinal eccentricity, which overcomes most of the previous existing limitations.

## 2. Methods

### 2.1. Experimental apparatus

The optical system's diagram is presented in Fig. 1. The apparatus employed only off-the-shelf components, and it was devised to operate in the human eye. The system included a wide field eyepiece (lenses L1-5) specifically designed and optimized for this apparatus by using a ray tracing program (OpticStudio 16, Zemax LLC, USA). The eye lens L1 is a positive meniscus of

100mm focal and 50 mm diameter (LE1076-B, Thorlabs Inc, USA), L2-L4 are identical doublets of 200 mm focal and 75 mm diameter (#88-596, Edmund Optics, UK). L5 is a negative singlet lens of -60 mm focal and 40 mm diameter (SLB-40-60NIR1, Optosigma Europe SAS, France). The eyepiece exhibited a back focal length of 37.6 mm. This distance is the clearance from the eyepiece to the plane where the entrance pupil of the eye must be placed for correct operation of the instrument. Lens L6 was a positive doublet of 75 mm focal and 50 mm diameter forming a telescope in combination with the compounded eyepiece. To operate in such telescopic manner, the focal point of L6 coincided with the virtual object focal point of the eyepiece. The latter was located at 28.1 mm away from the surface of L5. The next element in the system was a steering mirror SM (MR-15-30-PS-25 × 25D, Optotune Switzerland AG, Switzerland) located at the object focal plane of L6. With such design, the SM is optically conjugated with the entrance pupil of the eye. The mirror allowed a resolution of 22  $\mu$ rad, with a typical response time of 8 ms. The SM was the responsible of scanning a collimated narrow laser beam of 850 nm (#37-040, Edmund Optics, UK), limited at the exit of the source by a pupil of 0.8 mm diameter. Accounting for the magnification of the telescope formed by L6 and the eyepiece, the beam was 0.29 mm at the entrance pupil of the eye. The laser beam was introduced in the optical axis of the system by means of a non-polarizing 10/90 beam splitter (shown as BS in Fig. 1). The emission of the laser was attenuated with a neutral filter, not shown in the figure, so that energy of the beam at the entrance pupil was kept below 75  $\mu$ W, far below the maximum exposure limit. The SM scanned at any eccentricity within the operating range. In Fig. 1 different colors display angles of 11.5, 8.5, 6, and 3 deg from mirror, from top to the bottom, corresponding on the entrance pupil of the eye to 31.74, 23.4, 16.5, and 8.25 deg, respectively. The light back-reflected from the patient's retina followed the same trajectory and was de-scanned by the SM, resulting in a steady optical path towards the sensor for all beams containing phase information from the eye, independently of their angle at the pupil plane.

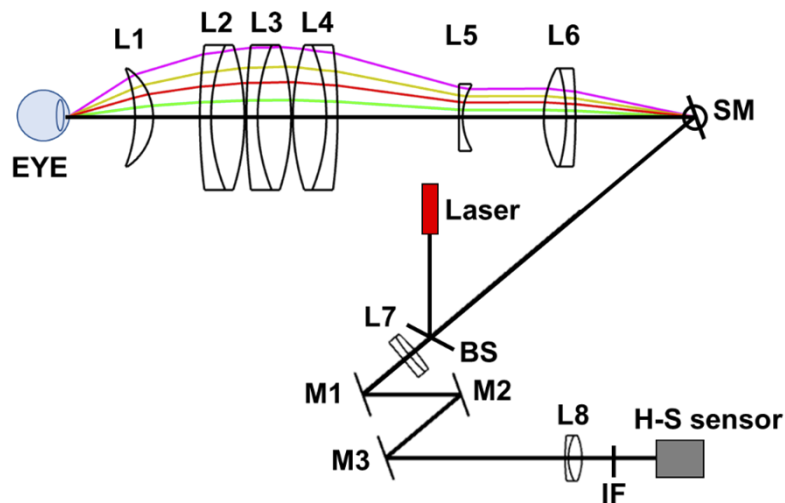


**Fig. 1.** Experimental apparatus showing the optical axis in solid black line and diverse optical elements. Trajectories in colors correspond to different scanning angles generated by the steering mirror (SM). Light backscattered from the retina is de-scanned so that the beam enters the sensor's relay steady along the optical axis. Folding mirrors M1-3 permit a compact design. An interference filter IF in front of the sensor selects light centered at 850 nm emitted by the laser. For more details and meaning of abbreviations in the figure see the main text.

The plane containing the SM was optically conjugated with the H-S wavefront sensor by means of a telescopic relay formed by lenses L7 (AC254-200-B, Thorlabs Inc, USA) and L8 (AC254-50-B, Thorlabs Inc, USA). The total magnification of the system, from the eye's entrance pupil to the plane of the sensor was 0.69.

The H-S wavefront sensor was compounded of an array of microlenses of 3.17 mm focal length and 192  $\mu\text{m}$  pitch (APO-Q-P192-F3.17, Flexible Optical B.V., Netherlands), and a CMOS camera (DMM 37UX252-ML, The Imaging Source Europe GmbH, Germany). An interference filter IF centered at 850 nm and with a 10 nm bandwidth (FBH850-10, Thorlabs Inc, USA) selected the light emitted by the laser.

Two CMOS cameras (DMM 72BUC02-ML, The Imaging Source Europe GmbH, Germany) 185 mm apart, evenly separated from the eye lens L1 in the horizontal meridian, served to center the subject to the system. Additionally, they were used to center external optical elements for alignment and calibration. The entrance pupil of the eye, given by the virtual image of the pupil generated by the cornea, must be located at the focal plane of the eyepiece and coincident with the optical axis of the apparatus for its optimal operation. By using the simultaneous images from the two cameras and applying straightforward triangulation, the clinician can accomplish precise 3D positioning of the eye, as described before [46].

The optics of the instrument was mounted on a  $300 \times 300\text{mm}$  breadboard occupying approximately half of its surface. A picture of the actual system is shown in panel (A) of Fig. 2. All the electronics and power supplies for the laser and cameras were placed around the optics, so that the full set could be enclosed in a single frame. The external cover was manufactured on a 3D printer in polylactic acid (PLA) material and mounted on a movable stage allowing 2D displacement in the horizontal plane, and vertical adjustment using a joystick. A chin rest and forefront served for subject's fixation. The system was connected to a single computer ready for operation in the clinic. Panel (B) of Fig. 2 shows a picture of the instrument once mounted and enclosed in the frame.

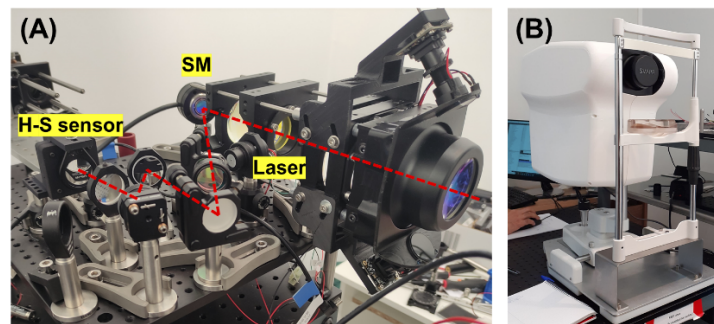


**Fig. 2.** (A) Picture of the actual optical system with its main components. The red dashed line indicates the light path across the apparatus. (B) Instrument enclosed in a frame for clinical use.

## 2.2. System calibration

The optical aberrations introduced by the system through different eccentricities were accounted for and subtracted in the wavefront sensor by means of a semi-empirical method. In a first stage, a collimated beam was introduced at different angles in 5 deg steps from the optical axis of the instrument, with the pivot point conjugated with the SM. Horizontal, vertical and the two oblique meridians were sampled. Zernike polynomials up to fifth order were determined from the recorded H-S images, corresponding to the intrinsic aberrations of the system for the sampled directions. To obtain semi-empirical mathematical functions for the system aberrations to be

compensated at any possible angle within the instrument range, the experimental values at the sampled points were fit to a 2-D polynomial of horizontal and vertical eccentricity for each individual Zernike term. In all cases, the correlation coefficient of the fitting stood above 0.95. Accordingly, during the operation of the system the so-obtained values for the set of polynomials at a given eccentricity were subtracted from the wavefront readouts, so that the output discharged the aberration contribution of the system.

Another type of aberration also introduced by the eyepiece that affected the output of the H-S sensor was image distortion. It manifests as a change in magnification across the field, typically as a function of the distance to the optical axis. Because of distortion, the pupil, and likewise the wavefront, projected onto the H-S were stretched mainly in a radial direction, by an amount proportional to the eccentricity. To illustrate the effect of this stretching, a circular pupil perpendicular to the path of light at a given eccentricity would appear as an ellipse elongated in radial direction on the HS plane, and a spherical wavefront impinging the ocular would have a longer radius of curvature in radial direction, thus appearing as a combination of defocus and astigmatism. Instead of altering the H-S processing algorithm to compensate for this wavefront distortion, we selected, for simplicity, to always process the H-S images on a fixed circular pupil regardless of eccentricity, and then apply a geometrical correction to the resulting Zernike coefficients, based on a simple model of distortion considering radial and tangential magnifications. To estimate these magnifications as a function of eccentricity, series of spherical trial lenses ranging from -10 D to +10 D were introduced at the pupil plane, perpendicular to the path of a collimated beam entering the system at different angles. Magnification values for each eccentricity were calculated by fitting from the measured defocus and astigmatism as a function of lens power. Finally, each set of magnification estimates, radial and tangential, was fitted to a circular paraboloid to produce the required parameters for Zernike coefficient conversion. These fittings corresponded to a first order approximation in a typical “even-order polynomial model” of distortion treatment [47]. The distortion was compensated at every eccentricity accordingly.

Because of the existing field aberrations in the eyepiece, the entrance pupil of the eye projected on the wavefront sensor drifted with eccentricity, with a maximum around 0.5 mm for 25 deg. This drift was calibrated and accounted for when processing H-S images at any given eccentricity.

### 2.3. Fixation and scanning

A visual stimulus was presented to the subject to keep a steady line of sight during the scanning of the laser beacon on the retina. The fixation target was produced by rapid rotation of the steering mirror itself, forming a flickering disc of 0.5 deg diameter. The stimulus was intermittently presented for 150 ms every 300 ms while the rest of the cycle was used to scan through eccentricities at 90 HZ to measure refraction/aberrations. The choice of the fixation target was made twofold: in one hand to keep a small stimulus so that foveal vision could be guaranteed, and in the other hand to assure as much as possible that the programmed eccentricities were applied by rapidly changing between fixation and refraction measurements. A custom software interface was developed to operate and control the instrument. The software incorporated different scanning protocols. The basic operation mode consisted of displaying the fixation circle on axis and sampling a circular retinal field of 50 deg in diameter following a square grid in 5 deg steps, completed in 3 sec. Combinations of scans with eccentric fixations allow extending the field. For example, by using 2 fixation orientations at  $\pm 15$  deg in horizontal meridian aberrations/refraction can be mapped on a  $70 \times 50$  deg retinal field. An additional pre-set mode allows a high-density sampling in steps of 1 deg along any selected retinal meridian. All changes in fixation could be accomplished by the steering mirror with no other movable part in the instrument. Measurements can be stored and combined from consecutive runs to enlarge the retinal field or to achieve higher resolution, keeping each scan under 3 sec as a rule.

Since the eyepiece is used in double pass to convey and collect light, when the scanning beam hits on the optical axis of the system, back reflections on its lenses dazzle the H-S sensor preventing its correct operation, creating a blind area of approximately 6 deg diameter. Outside this zone, back reflections from the instrument did not affect its performance. Corneal reflections occasionally appearing for some subjects and angles were compact, since the beam at the corneal plane was just 0.29 mm wide and therefore, only a small fraction of the total number of spots in the H-S images were affected. The software package performed routine checking of each spot quality (morphology, intensity, and signal-to-noise ratio) and discarded non-compliant ones, so that modal estimation of the wavefront or refraction was not compromised.

#### 2.4. Protocol for experimental measurements

To assess the accuracy of the apparatus, set of trial lenses with known values of defocus and astigmatism were measured in the system. The lenses were placed in a dedicated holder designed to maintain them steady, still allowing the controlled rotation around the pivot point in front of the system. The sensitivity of the reticle on the rotating wheel of the holder was 1 deg. A collimated beam from a diode laser source emitting at 785 nm (S1FC780, Thorlabs Inc, USA) back illuminated the lenses and moved together with them in the rotation. Collimation of the beam (F810APC-780, Thorlabs Inc, USA) was set prior to its use by using a shearing interferometer. The orientation of the astigmatic lenses was adjusted manually by means of an angle conveyor with 1 deg sensitivity. The trial lenses were measured for different meridians and eccentricities ranging from 0 to 25 deg.

To test the instrument in real eyes, 11 volunteers (mean age  $36 \pm 10$  years, mean refraction  $-2.8 \pm 1.8$  D) were examined. The participants were free from any ocular pathology and exhibited normal vision. No constraint was placed on age or refraction in the study. The subjects underwent different scanning protocols to test the instrument. The recruitment of participants followed the tenets of the Helsinki declaration and adhered to the ethical protocols approved by the institution pertaining this project.

### 3. Results

#### 3.1. Trial lenses

The first testing consisted of measuring the set of spherical trial lenses with power ranging from -10 to 10 D and placed perpendicular to the path of light for eccentricities in 5-deg steps along four meridians: vertical, horizontal, and  $\pm 45^\circ$  oblique directions. Lenses were mounted on a dedicated holder as it was disclosed in previous section. Figure 3 displays a selection of the results corresponding to the positive vertical eccentricities, presented in different panels.

Linear fitting of the measured refraction versus lens power yielded slope values very close to the ideal value, -1, and determination coefficients,  $R^2$ , above 0.999 in all cases. The application of negative lenses of power produced a measured positive value of defocus and vice versa, in accordance with the sign convention in optometric practice.

Panel A in Fig. 4 presents a summary of the results for spherical trial lenses. It shows the mean defocus for each lens power, averaging across different meridians and eccentricities. Error bars correspond to standard deviation for each data point. The average standard deviation across eccentricities was 0.19 D.

The system was further tested by using astigmatic trial lenses of power -4, -2, 2, and 4 D. These lenses were rotated to orientations 0, 45, 90, and 135 deg with the horizontal direction as reference origin (0 deg). Panel (B) in Fig. 4 shows the experimental results for the dioptric power of the signed astigmatic lenses (dots). Error bars corresponding to the standard deviation (mean value 0.15D) are barely visible for they are contained in the points. The linear fit exhibited a virtually perfect  $R^2 = 1$ , with a slope superior to 0.99 in absolute value.

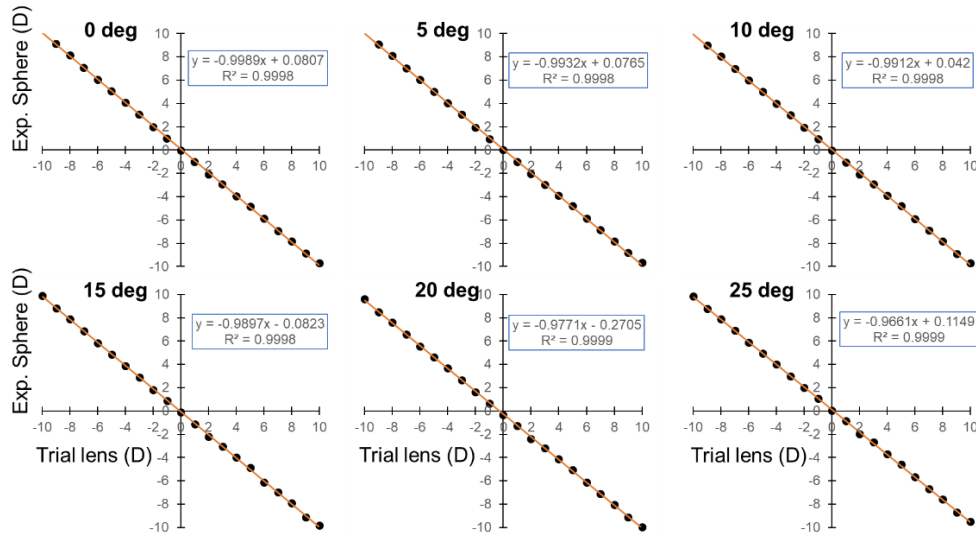


**Fig. 3.** Experimental defocus along the positive vertical direction for the set of trial lenses (black dots). Linear fitting is shown with a red line. The linear equation estimated from the fitting is presented at every panel.

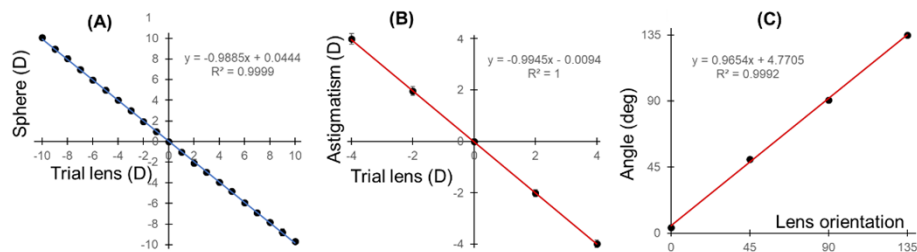


**Fig. 4.** (A) Average measured defocus across eccentricities as a function of spherical trial lens power. (B) Average signed astigmatism measured across eccentricities as a function of cylindrical trial lens power. (C) Average, across eccentricities and lens power values, of the estimated orientation of the astigmatic lenses. In all the panels a linear fit of the experimental data is presented. Error bars corresponding to the standard deviation lie below the size of the points.

The estimation of the rotated angles of the astigmatic trial lenses is presented in panel (C) of Fig. 3. In this case, the mean standard deviation was 1.8 deg. The error bars lie below the size of the black dots corresponding to the experimental results; therefore, they remain hidden in the scale of the figure.

### 3.2. Real eyes

The basic operation mode, consisting of scanning a circular retinal field of 50 deg of diameter in a rectangular grid with 5-deg steps, was first applied to study the repeatability of the output in all subjects. Three consecutive runs of the basic scanning protocol were acquired for each volunteer's right eye. The spherical equivalent refraction (SER) was calculated at every sampled point of the retina across the field. In Fig. 5, the standard deviation obtained from 3 runs is presented for this scanning mode together with a color-coded representation of the spherical equivalent refraction in two subjects.

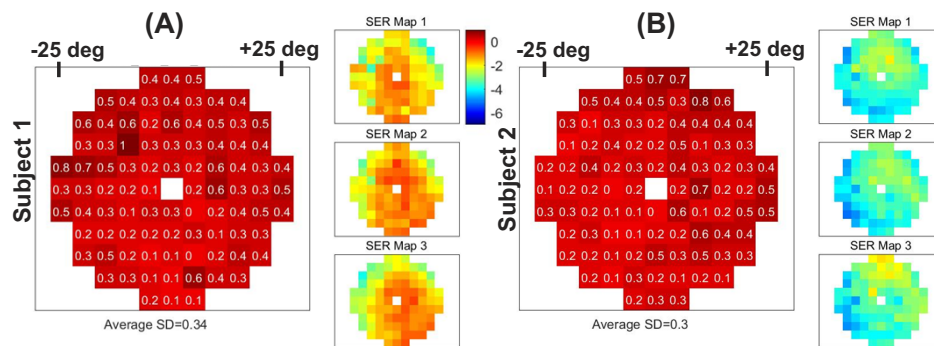


**Fig. 5.** The larger panels show the standard deviation obtained at every eccentricity with the basic scanning protocol through 3 consecutive runs in 2 subjects. Numerical values are provided at any point in diopters. The spherical equivalent refraction (SER) maps from the 3 runs are shown in the columns. The same color code is used in all panels. Mean standard deviation, obtained by averaging each standard deviation map is given at the bottom.

In every plot, right and left sides correspond to temporal and nasal retina, and up and down to superior and inferior retina, respectively. Average standard deviation is presented below each panel. When repeating the process for all subjects, a mean variation of 0.35 D was a found across eccentricities.

As an aid to visual interpretation of results, the outcomes of a 2-D scan across eccentricities can be represented as color-coded maps. Besides SER, as in both columns in Fig. 5, the custom software can produce maps showing sphere, cylinder, and horizontal/vertical and oblique Jackson crossed cylinders, J0 and J45. Figure 6 shows examples of these maps in 3 subjects, with a protocol combining 3 scans with fixation at 0 and  $\pm 15$  deg in the horizontal meridian. In the overlapping areas, average values were calculated across scans. Color codes for retinal dioptric power are the same in all panels, ranging from -4 (red) to 4 D (blue). The numerical value is superimposed at each data point.

Isolated values significantly different than their neighbors can be found in some scans, as is the case for Subjects 3 and 5 around 15-20 deg nasal, 5 deg superior. It was frequent to find this type of artifact, which can probably be attributed to the optic disc, as it lies about this retinal eccentricity. Neither these nor any other freak values have been eliminated from the maps since they constituted a small fraction of the retinal eccentricities at most and can be easily discarded if necessary. The difference in SER relative to foveal refraction is presented in Fig. 7 for several

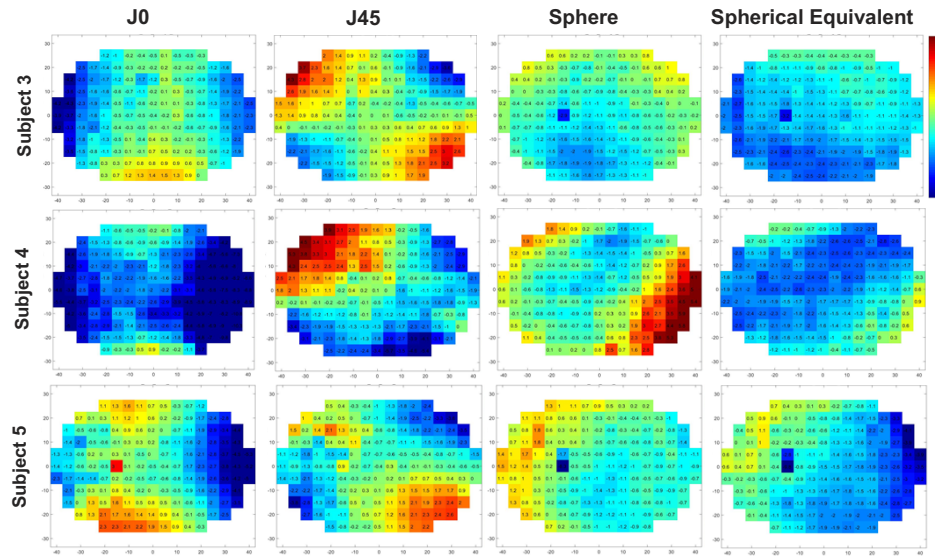


**Fig. 6.** Peripheral refraction maps in terms of Jackson crossed cylinders J0 and J45, sphere, and spherical equivalent refraction, obtained by combining 3 fixation points at 0,  $\pm 15$  deg for 3 subjects. All maps have the same color coding, shown in the color bar. The scanning time for each fixation was below 3 sec. Mean values were calculated for eccentricities covered with more than one fixation. Numerical values in diopters are superimposed at each eccentricity. Adjacent squared cells are separated by 5 deg in every direction.

subjects. This kind of map is particularly useful to better compare retinal morphology across subject with, e.g., different refractive errors.

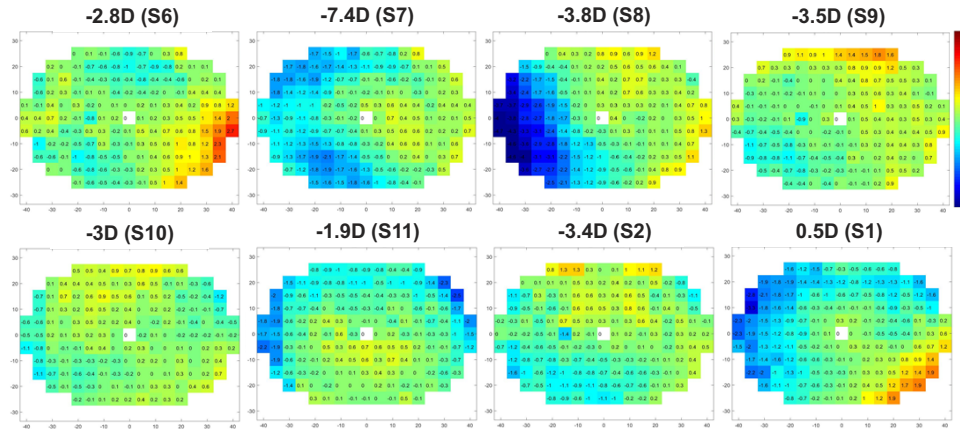


**Fig. 7.** Relative spherical equivalent peripheral refraction, with reference in central fovea, obtained by combining 3 fixation points at 0,  $\pm 15$  deg for 8 subjects. Foveal SER for each subject is provided above each panel, together with the identification code of the subject. All maps have the same color coding, shown in the colorbar. The scanning time for each fixation was below 3 sec. Mean values were calculated for eccentricities covered with more than one fixation. Numerical values in diopters are superimposed at each eccentricity.

Foveal refraction and subject ID are given on top of each panel in Fig. 7. All retinal refractions are represented with the same color code, ranging from -4 to 4 D. The foveal data point was left in white color for a better visual identification of the central retina position.

#### 4. Discussion

Lenses L1 to L6 were a combination of doublets and singlets. Different lens models are commercially available with the same focal lengths and diameters but better performance and optical quality. Nevertheless, the selection presented here exhibited a critical advantage in comparison with other possible arrangements in terms of back reflections of the scanned laser beam. In some cases, these unwanted reflections were several orders of magnitude brighter on the wavefront sensor than the signal received from the eye, therefore preventing the system from proper operation. Current antireflection coatings did not circumvent the problem, since the reflected intensity was still far higher than the one coming from the patient's retina. The solution for the instrument presented in this work consisted of choosing lenses with geometries that avoided back reflections coaxial to the incidence beam. To get this effect, the incoming beam was prevented from hitting any lens surface in a direction pointing to its center of curvature. With this approach, there was still an unavoidable back reflection when the scanned beam entered L6 and the eyepiece through the optical axis. This fact does not limit the system in practice, since central refraction can be obtained by setting the fixation point off-axis. The back reflection on axis could be further limited by narrowing the beam. In the system presented in this work, with the given beam diameter, the blind zone because of on-axis reflection comprised approximately 6 deg ( $\pm 3$  deg).

In practice, scanning angles through the eyepiece were limited by lens holders to a portion of the usable diameter. In addition, the wavefront coming back from the eye was wider than the incident beam. The wavefront estimation was accomplished by a standard modal algorithm, so a portion of the beam would be enough, at least theoretically, to estimate spherical equivalent across the entire beam. Nevertheless, for the sake of precision the range was constrained to  $\pm 25$  deg in the vertical and horizontal meridians so that through the scan a pupil at least 3 mm in diameter was always fully available in the sensor for processing. By changing the fixation point, or adding more than one point, this field has been shown to increase without other technical difficulties but increasing the time of measurement.

The measurement of trial lenses was required to test the performance of the instrument, both hardware and software. From the results shown in Figs. 3 and 4, it can be concluded that the instrument is able to estimate defocus and astigmatism with high accuracy, since the slope of the linear fitting between lens power and measured refractive error is very close to the ideal -1 and there is virtually no offset in either case. Concerning precision, average standard deviations were 0.19 D and 0.15 D in the magnitude of sphere and astigmatic power, respectively. Regarding cylinder axis, average standard deviation was 1.8 deg, while the linear polynomial fitting in panel (C), Fig. 4 shows an offset of 4.77 deg. This bias is hardly relevant from a clinical perspective, and it can be easily corrected in the results, but we suspect it to be due to a tilt of the platform where the trial lenses were positioned. Although already clinically good, the accuracy of the instrument it can be further improved by developing calibration protocols which guarantee better alignment between trial lenses and instrument, and by using a more precise set of lenses instead of standard trial lenses.

When testing repeatability in the instrument, the standard deviation of SER along 3 scans in the same subject was 0.35 D on average across eccentricities and subjects. This variability can be due to several factors. One of them is the initial centering of the subject to the instrument. Although the double camera system allowed high precision, the user must perform the operation carefully to attain similar positions across runs. Other potential sources of uncertainty in the results came from the patient. The instrument requires the subject to maintain fixation

on the test during the scan, and therefore, results may fluctuate with the subject's ability to do so. Additionally, accommodation fluctuations naturally change the eye's refraction and, accordingly, the instrument outcomes. Consequently, young subjects should present larger uncertainty in the results under natural vision conditions. The mean age of the subjects in this work was  $36 \pm 10$  years, ranging from 26 to 60. Consequently, while some subjects maintained a significant amplitude of accommodation, others were fully presbyopic. In any case, the average standard deviation found is within the range of fluctuations in accommodation for young subjects, suggesting this to be the main source of variability in the measurements. Better results could be obtained by paralyzing accommodation, which in addition it would prevent the appearance of instrument myopia.

The instrument operated under quite different refractions, as it was presented in Figs. 6 and 7. Nevertheless, a characterization of the retinal morphology as a function of SER was out of the scope of this work. The number of subjects was low, with ages spanning a wide range, to infer any conclusion in this regard. The instrument was shown capable for such task, although in the present work we focused on studying and characterizing its performance.

## 5. Conclusions

We present a new instrument for fast, programmable 2D measurement of refraction and aberrations of the whole human retina in a wide range of eccentricities. A major advantage of the apparatus is its accuracy and fast operation time, allowing to scan near 100 points for a single fixation in a circle of 50 deg diameter on the retina in less than 3 sec. By combining this basic operation mode with different fixation points, expanded fields can be measured. The instrument passed a thorough calibration, showing high accuracy. A group of participants of varying ages and central refractions underwent different scanning protocols to demonstrate the versatility of the apparatus. The variability of refraction across the field in real eyes was 0.35 D, comparable to any non-cyclopegic current technique. The instrument provides an unprecedented tool for the investigation of peripheral refraction that might give a new insight into basic questions such as the emmetropization process or myopia control. Due to its robust operation and simplicity, the apparatus can be employed in large populations efficiently in clinical environments.

**Funding.** Intramural grant by Aier Eye Hospital Group (AR1903D2); Key Project of Research and Development Plan of Hunan Province (2019SK2051); Fundación Séneca (19897/GERM/15); Agencia Estatal de Investigación (PID2019-105684RB-I00/AEI/10.13039/501100011033).

**Disclosures.** Some of the authors are co-inventors in a patent application of the described instrument.

**Data availability.** Data underlying the results from measurements of trial lenses and subjects presented in this paper are not publicly available, but it may be obtained from the corresponding author upon reasonable request.

## References

1. J. M. Wood and R. Troutbeck, "Effect of restriction of the binocular visual field on driving performance," *Ophthalmic. Physiol. Opt.* **12**(3), 291–298 (1992).
2. C. Owsley and G. McGwin Jr, "Vision impairment and driving," *Surv. Ophthalmol.* **43**(6), 535–550 (1999).
3. B. Wolfe, J. Dobres, R. Rosenholtz, and B. Reimer, "More than the useful field: considering peripheral vision in driving," *Appl. Ergon.* **65**, 316–325 (2017).
4. C. M. Patino, R. McKean-Cowdin, S. P. Azen, J. C. Allison, F. Choudhury, and R. Varma, "Central and peripheral visual impairment and the risk of falls and falls with injury," *Ophthalmology* **117**(2), 199–206.e1 (2010).
5. J. Källstrand-Eriksson, A. Baigi, N. Buer, and C. Hildingh, "Perceived vision-related quality of life and risk of falling among community living elderly people," *Scand. J. Caring Sci.* **27**(2), 433–439 (2013).
6. C. O'Connell, A. Mahboobin, S. Drexler, M. S. Redfern, S. Perera, A. C. Nau, and R. Cham, "Effects of acute peripheral/central visual field loss on standing balance," *Exp. Brain Res.* **235**(11), 3261–3270 (2017).
7. N. Schumacher, M. Schmidt, R. Reer, and K. M. Braumann, "Peripheral vision tests in sports: training effects and reliability of peripheral perception test," *Int. J. Environ. Res. Public Health* **16**(24), 5001 (2019).
8. A. Klostermann, C. Vater, R. Kredel, and E. J. Hossner, "Perception and action in sports. On the functionality of foveal and peripheral vision," *Front. Sports Act. Living* **1**, 66 (2020).

9. L. Tarita-Nistor, E. G. González, S. N. Markowitz, L. Lillakas, and M. J. Steinbach, "Increased role of peripheral vision in self-induced motion in patients with age-related macular degeneration," *Invest. Ophthalmol. Visual Sci.* **49**(7), 3253–3258 (2008).
10. J. B. Hassell, E. L. Lamoureux, and J. E. Keefe, "Impact of age related macular degeneration on quality of life," *Br. J. Ophthalmol.* **90**(5), 593–596 (2006).
11. K. Baskaran, R. Rosén, P. Lewis, P. Unsbo, and J. Gustafsson, "Benefit of adaptive optics aberration correction at preferred retinal locus," *Optom. Vis. Sci.* **89**(9), 1417–1423 (2012).
12. L. Lundström, J. Gustafsson, and P. Unsbo, "Vision evaluation of eccentric refractive correction," *Optom. Vis. Sci.* **84**(11), 1046–1052 (2007).
13. P. K. Verkicharla, A. Mathur, E. A. Mallen, J. M. Pope, and D. A. Atchison, "Eye shape and retinal shape, and their relation to peripheral refraction," *Ophthalmic Physiol. Opt.* **32**(3), 184–199 (2012).
14. J. M. Pope, P. K. Verkicharla, F. Sepehrband, M. Suheimat, K. L. Schmid, and D. A. Atchison, "Three-dimensional MRI study of the relationship between eye dimensions, retinal shape and myopia," *Biomed. Opt. Express* **8**(5), 2386–2395 (2017).
15. D. A. Atchison, N. Pritchard, K. L. Schmid, D. H. Scott, C. E. Jones, and J. M. Pope, "Shape of the retinal surface in emmetropia and myopia," *Invest. Ophthalmol. Visual Sci.* **46**(8), 2698–2707 (2005).
16. W. N. Charman and H. Radhakrishnan, "Peripheral refraction and the development of refractive error: a review," *Ophthalmic Physiol. Opt.* **30**(4), 321–338 (2010).
17. W. Lan, Z. Lin, Z. Yang, and P. Artal, "Two-dimensional peripheral refraction and retinal image quality in emmetropic children," *Sci. Rep.* **9**(1), 16203 (2019).
18. C. E. Ferree, G. Rand, and C. Hardy, "Refraction for the peripheral field of vision," *Arch. Ophthalmol.* **5**(5), 717–731 (1931).
19. L. Ronchi, "Absolute threshold before and after correction of oblique-ray astigmatism," *J. Opt. Soc. Am.* **61**(12), 1705–1709 (1971).
20. L. Lundström, J. Gustafsson, I. Svensson, and P. Unsbo, "Assessment of objective and subjective eccentric refraction," *Optom. Vis. Sci.* **82**(4), 298–306 (2005).
21. D. W. Jackson, E. A. Paysse, K. R. Wilhelmus, M. A. Hussein, G. Rosby, and D. K. Coats, "The effect of off-the-visual-axis retinoscopy on objective refractive measurement," *Am. J. Ophthalmol.* **137**(6), 1101–1104 (2004).
22. F. Rempt, J. Hoogerheide, and W. P. H. Hoogenboom, "Peripheral retinoscopy and the skiagram," *Ophthalmologia* **162**(1), 1–10 (1971).
23. W. Lotmar and T. Lotmar, "Peripheral astigmatism in the human eye: experimental data and theoretical model predictions," *J. Opt. Soc. Am.* **64**(4), 510–513 (1974).
24. J. Santamaría, P. Artal, and J. Bescós, "Determination of the point-spread function of human eyes using a hybrid optical-digital method," *J. Opt. Soc. Am. A* **4**(6), 1109–1114 (1987).
25. J. A. Jennings and W. N. Charman, "Optical image quality in the peripheral retina," *Am. J. Optom. Physiol. Opt.* **55**(8), 582–590 (1978).
26. R. Navarro, P. Artal, and D. R. Williams, "Modulation transfer of the human eye as a function of retinal eccentricity," *J. Opt. Soc. Am. A* **10**(2), 201–212 (1993).
27. P. Artal, S. Marcos, R. Navarro, and D. R. Williams, "Odd aberrations and double-pass measurements of retinal image quality," *J. Opt. Soc. Am. A* **12**(2), 195–201 (1995).
28. A. Guirao and P. Artal, "Off-axis monochromatic aberrations estimated from double pass measurements in the human eye," *Vision Res.* **39**(2), 207–217 (1999).
29. A. Seidemann, F. Schaeffel, A. Guirao, N. Lopez-Gil, and P. Artal, "Peripheral refractive errors in myopic, emmetropic, and hyperopic young subjects," *J. Opt. Soc. Am. A* **19**(12), 2363–2373 (2002).
30. M. C. M. Dunne, G. P. Misson, E. K. White, and D. A. Barnes, "Peripheral astigmatic asymmetry and angle alpha," *Ophthalmic Physiol. Opt.* **13**(3), 303–305 (1993).
31. D. A. Atchison, N. Pritchard, and K. L. Schmid, "Peripheral refraction along the horizontal and vertical visual fields in myopia," *Vision Res.* **46**(8-9), 1450–1458 (2006).
32. N. S. Logan, B. Gilmartin, C. F. Wildsoet, and M. C. Dunne, "Posterior retinal contour in adult human anisomyopia," *Invest. Ophthalmol. Visual Sci.* **45**(7), 2152–2162 (2004).
33. W. N. Charman and J. A. M. Jennings, "Longitudinal changes in peripheral refraction with age," *Ophthalmic Physiol. Opt.* **26**(5), 447–455 (2006).
34. J. Gustafsson and P. Unsbo, "Eccentric correction for off-axis vision in central visual field loss," *Optom. Vis. Sci.* **80**(7), 535–541 (2003).
35. P. M. Prieto, F. Vargas-Martín, S. Goelz, and P. Artal, "Analysis of the performance of the Hartmann-Shack sensor in the human eye," *J. Opt. Soc. Am. A* **17**(8), 1388–1398 (2000).
36. D. Romashchenko and L. Lundström, "Dual-angle open field wavefront sensor for simultaneous measurements of the central and peripheral human eye," *Biomed. Opt. Express* **11**(6), 3125–3138 (2020).
37. D. A. Atchison, D. H. Scott, and W. N. Charman, "Hartmann-Shack technique and refraction across the horizontal visual field," *J. Opt. Soc. Am. A* **20**(6), 965–973 (2003).
38. D. A. Atchison, "Comparison of peripheral refractions determined by different instruments," *Optom. Vis. Sci.* **80**(9), 655–660 (2003).

39. B. Jaeken, J. Tabernero, F. Schaeffel, and P. Artal, "Comparison of two scanning instruments to measure peripheral refraction in the human eye," *J. Opt. Soc. Am. A* **29**(3), 258–264 (2012).
40. L. Lundström, S. Manzanera, P. M. Prieto, D. B. Ayala, N. Gorceix, J. Gustafsson, P. Unsbo, and P. Artal, "Effect of optical correction and remaining aberrations on peripheral resolution acuity in the human eye," *Opt. Express* **15**(20), 12654–12661 (2007).
41. X. Wei and L. Thibos, "Design and validation of a scanning Shack Hartmann aberrometer for measurements of the eye over a wide field of view," *Opt. Express* **18**(2), 1134–1143 (2010).
42. B. Jaeken, L. Lundström, and P. Artal, "Fast scanning peripheral wave-front sensor for the human eye," *Opt. Express* **19**(8), 7903–7913 (2011).
43. B. Jaeken and P. Artal, "Optical quality of emmetropic and myopic eyes in the periphery measured with high-angular resolution," *Invest. Ophthalmol. Visual Sci.* **53**(7), 3405–3413 (2012).
44. Z. Lin, R. Duarte, S. Manzanera, W. Lan, P. Artal, and Z. Yang, "Two-dimensional peripheral refraction and retinal image quality in orthokeratology lens wearers," *Biomed. Opt. Express* **11**(7), 3523–3533 (2020).
45. R. C. Bakaraju, C. Fedtke, K. Ehrmann, D. Falk, V. Thomas, and B. A. Holden, "Peripheral refraction and higher-order aberrations with cycloplegia and fogging lenses using the BHVI-EyeMapper," *J. Optom.* **9**(1), 5–12 (2016).
46. H. Ginis, O. Sahin, A. Pennos, and P. Artal, "Compact optical integration instrument to measure intraocular straylight," *Biomed. Opt. Express* **5**(9), 3036–3041 (2014).
47. F. Bukhari and M. N. Dailey, "Automatic radial distortion estimation from a single image," *J. Math. Imaging Vis.* **45**(1), 31–45 (2013).